Supporting Information

Plasma-Engineered NiO Nanosheets with Enriched Oxygen Vacancies for Enhanced Electrocatalytic Nitrogen Fixation

Yu-biao Li [#], Ya-ping Liu [#], Jing Wang, Ya-li Guo, Ke Chu *

School of Materials Science and Engineering, Lanzhou Jiaotong University, Lanzhou 730070, China

*Corresponding author. E-mail address: chukelut@163.com (K. Chu)

[#] These authors contributed equally to this work.

Experimental section

Synthesis of NiO/CC and P-NiO/CC

All the chemicals were used as received without further purification. The NiO nanosheet array on carbon cloth (NiO/CC) was prepared by a hydrothermal method[1]. Briefly, a piece of as-obtained CC (2 cm × 2 cm) was ultrasonically cleaned in concentrated HCl for 30 min, and washed with ethanol and distilled water several times. Then a 30 mL of aqueous solution containing 3 mmol of $Ni(NO_3)_2$ and 8 mmol of hexamethylene tetramine (HMT) was prepared and transferred into a 50 mL of Teflon-lined stainless-steel autoclave, followed by immersing the pre-treated CC into the autoclave. Afterwards, the autoclave was sealed and kept at 120 °C for 8 h and then naturally cooled down to room temperature. The obtained CC sample was annealed at 300 °C for 2 h at the heating rate of 3 °C min^{-1} under Ar atmosphere to acquire NiO/CC. Plasma treatment was performed on an AX-1000 plasma system with a radiofrequency power generator (13.56 MHz) at room temperature. The NiO/CC was treated by Ar plasma for 100-300s at a radiofrequency power of 100 W in Ar gas (flow rate: 10 sccm) to obtain P-NiO/CC. Unless otherwise specified, P-NiO/CC represents the sample treated for 200 s.

Electrochemical measurements

Electrochemical measurements were carried out using a standard three-electrode system on CHI-660E electrochemical workstation at ambient conditions. NiO/CC and P-NiO/CC (1 cm × 1 cm) were directly used as the working electrodes. The graphite rod and Ag/AgCl were used as the counter electrode and reference electrode, respectively. All potentials were referenced to the reversible hydrogen electrode (RHE) through $E_{RHE} = E_{Ag/AgCl} + 0.197 + 0.059 \times pH$. The NRR test was performed using an H-type two-compartment electrochemical cell separated by Nafion 115 membrane. The Nafion membrane was pretreated by boiling it in 5% H_2O_2 solution for 1 h, 0.5 M H_2SO_4 for 1 h and deionized water for 1 h in turn. Prior to NRR test, the electrolyte was purged with Ar for 30 min. During the electrolysis, N_2 gas (99.999% purity) was continuously fed into the cathodic compartment at a

flow rate of 10 mL min^{-1}, and the electrolyte in the cathodic compartment was subjected to magnetic stirring at a rate of 300 rpm throughout the measurement. The NH_3 yield and FE were determined by an indophenol blue method (Fig. S6 and Fig. S9 for details), and the N_2H_4 concentration was determined by a method of Watt and Chrisp (Fig. S7 for details).

Characterizations

Scanning electron microscopy (SEM) was conducted on a JSM-6701 microscope. Transmission electron microscopy (TEM) and high resolution transmission electron microscopy (HRTEM) were performed on a Tecnai G^2 F20 microscope. X-ray diffraction (XRD) pattern was taken on a 7000LX powder diffractometer. X-ray photoelectron spectroscopy (XPS) analysis was conducted on a PHI 5702 spectrometer. Raman spectra were recorded on a JY-HR800 Raman spectroscope. ^1H (NMR) spectra were collected on a 500 MHz Bruker superconducting-magnet NMR spectrometer. Electron paramagnetic resonance (ESR) measurements were acquired on an X-band spectrometer (Bruker ESP-300). Nitrogen adsorption/desorption isotherms were performed on an ASAP 2020 instrument. Temperature-programmed desorption (TPD) profiles were recorded on a Chem-BET 3000 (Quantachrome) apparatus.

Calculation details

Density functional theory calculations were carried out using a Cambridge sequential total energy package (CASTEP)[2]. Perdew-Burke-Ernzerhof (PBE) functional of generalized gradient approximation (GGA) was applied to describe the exchange correlation interaction[3]. The Hubbard *U* value of Ni atom was set to 6.5 eV. DFT-D correction was considered for van der Waals forces. During the geometry optimization, we set a cutoff energy of 650 eV and a Monkhorst mesh of 3 × 3 × 1. The energy and force were converged to 10^{-5} eV/atom and 0.005 eV/Å, respectively. Since the NiO (111) was reported to be most stable[4, 5], and it was also a dominated crystal face (as confirmed by our HRTEM analysis), the NiO (111) is explored for slab modeling. The six-layer NiO (111) slab (3×3 supercell) was constructed, in which the bottom three layers were fixed. A vacuum region of 15 Å was set to

separate adjacent slabs.

The adsorption energy (ΔE) is calculated as [6]

$$\Delta E = E_{\mathrm{ads/slab}} - E_{\mathrm{ads}} - E_{\mathrm{slab}} \tag{4}$$

where $E_{\mathrm{ads/slab}}$, E_{ads} and E_{slab} are the total energies for adsorbed species on slab, adsorbed species and isolated slab, respectively.

The Gibbs free energy (ΔG, 298 K) of the NRR intermediates is defined as [6]

$$\Delta G = \Delta E + \Delta ZPE - T\Delta S \tag{3}$$

where ΔE is the adsorption energy, ΔZPE is the zero point energy difference and $T\Delta S$ is the entropy difference between the gas phase and adsorbed state.

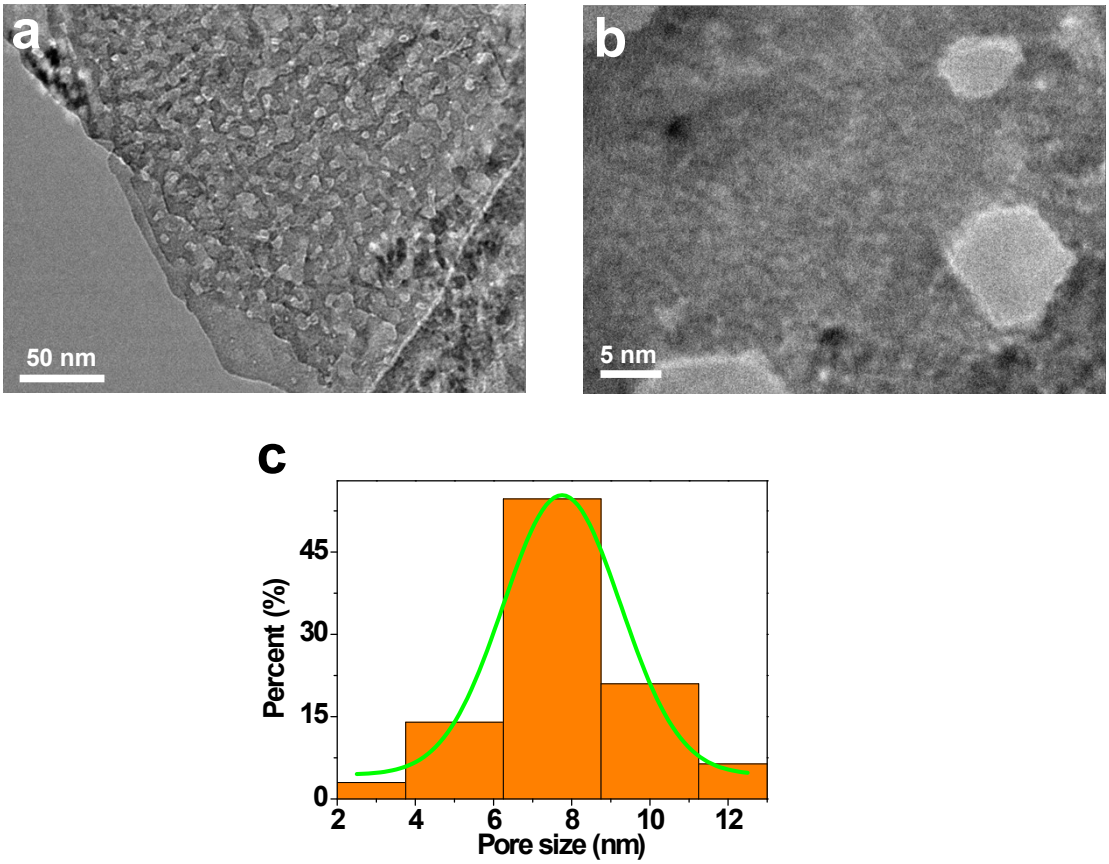

Fig. S1. (a) TEM and (b) HRTEM images of P-NiO nanosheets. (c) Pore size distribution of polygonous nanoholes on P-NiO nanosheets.

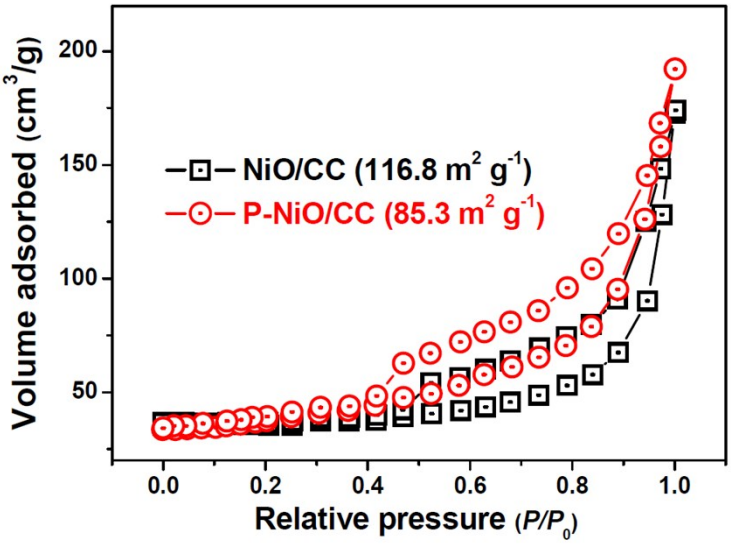

Fig. S2. Nitrogen adsorption/desorption isotherm curves of NiO/CC and P-NiO/CC.

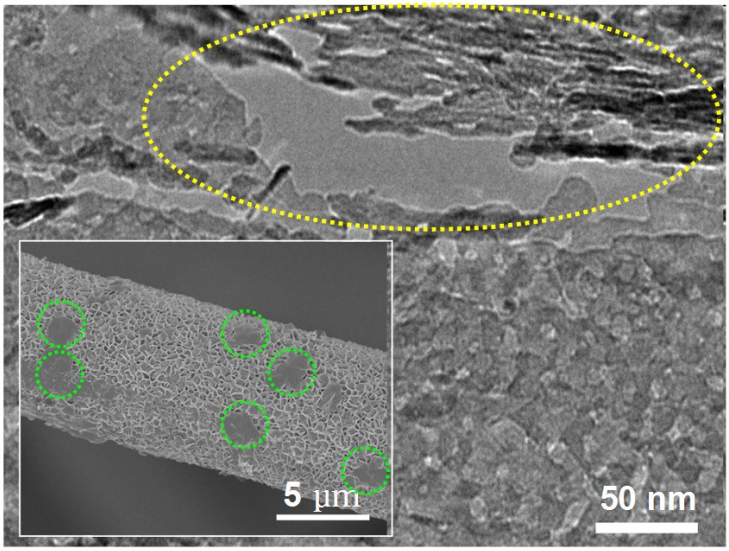

Fig. S3. Morphologies of P-NiO/CC after 300s plasma treatment. Obviously, overtreatment can break the nanosheets (yellow circle) and make some nanosheets peel off from the local areas of CC (green circles).

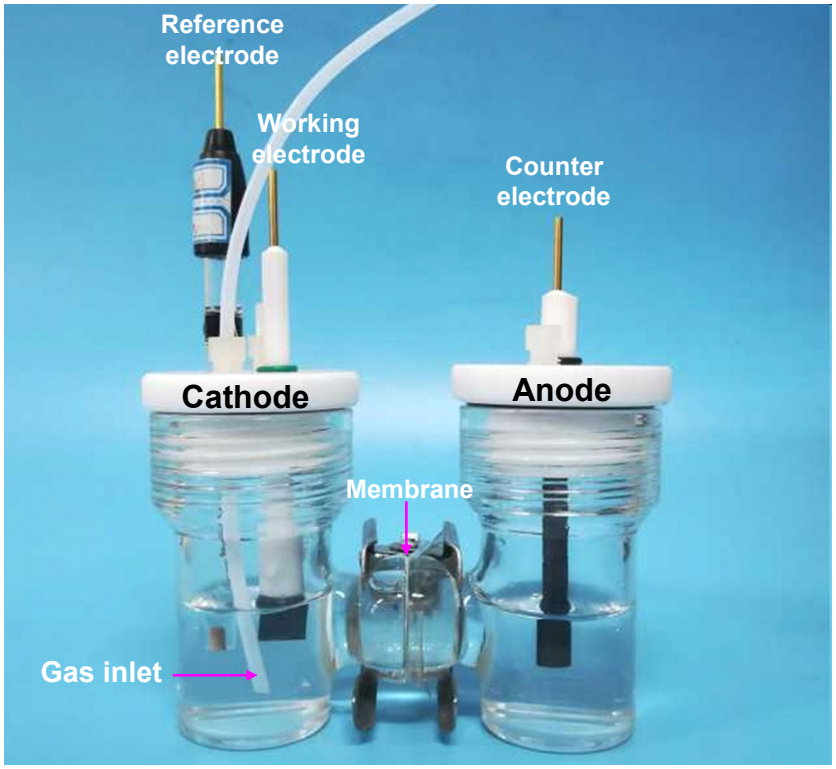

Fig. S4. Photograph of H-type electrochemical setup.

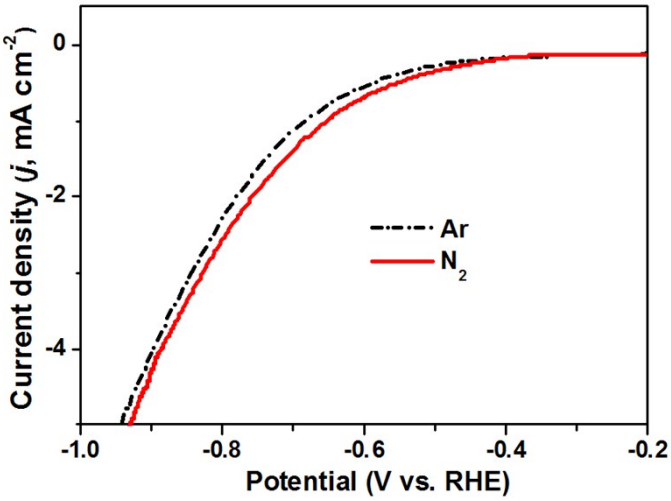

Fig. S5. LSV curves of P-NiO/CC in Ar- and N_2- saturated solutions.

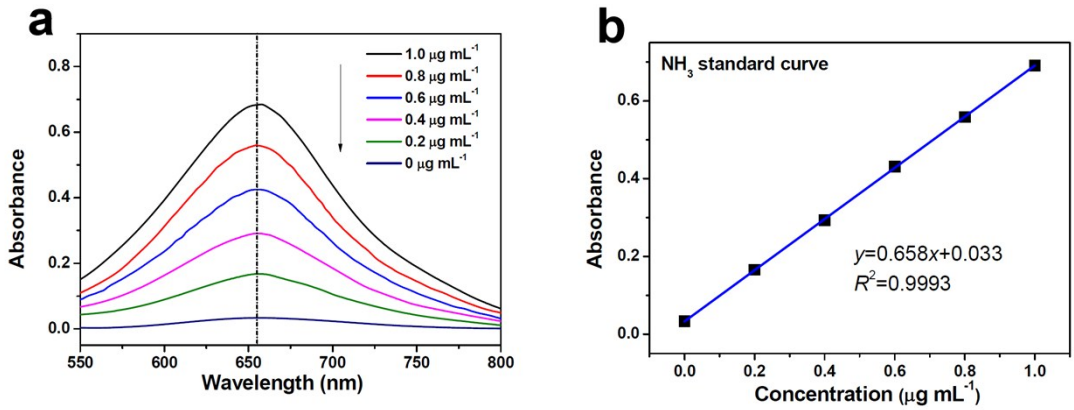

Fig. S6. (a) UV-Vis absorption spectra of indophenol assays with NH_4Cl in 0.1 M Na_2SO_4 after incubated for 2 h at ambient conditions. (b) Calibration curve used for calculation of NH_3 concentrations.

Determination of NH_3 in 0.1 M Na_2SO_4

The concentration of produced NH_3 in 0.1 M Na_2SO_4 was quantitatively determined by an indophenol blue method[7]. Typically, 4 mL of electrolyte was removed from the electrochemical reaction vessel. Then 50 μL of solution containing NaOH (0.75 M) and NaClO (ρ_{Cl} = ~4), 500 μL of solution containing 0.32 M NaOH, 0.4 M $C_7H_6O_3$, and 50 μL of $C_5FeN_6Na_2O$ solution (1 wt%) were respectively added into the electrolyte. After standing for 2 h, the UV-Vis absorption spectrum was measured and the concentration-absorbance curves were calibrated by the standard NH_4Cl solution with a serious of concentrations (Fig. S6a). As shown in Fig. S6b, the calibration curve shows a good linear relationship (y=0.658x+0.033, R^2 =0.9993)

NH_3 yield is calculated by

$$\text{NH}_3 \text{ yield } (\mu\text{g h}^{-1}\text{ mg}^{-1}) = \frac{C_{\text{NH}_3} \times V}{t \times m} \tag{S1}$$

Faradaic efficiency is calculated by

$$\text{Faradaic efficiency } (\%) = \frac{3 \times F \times c_{\text{NH}_3} \times V}{17 \times Q} \times 100\% \tag{S2}$$

where C_{NH3} is the measured NH_3 concentration, V is the volume of the electrolyte, t is the reduction time, m is the mass loading of catalyst on carbon paper, F is the Faraday constant and Q is the quantity of applied electricity.

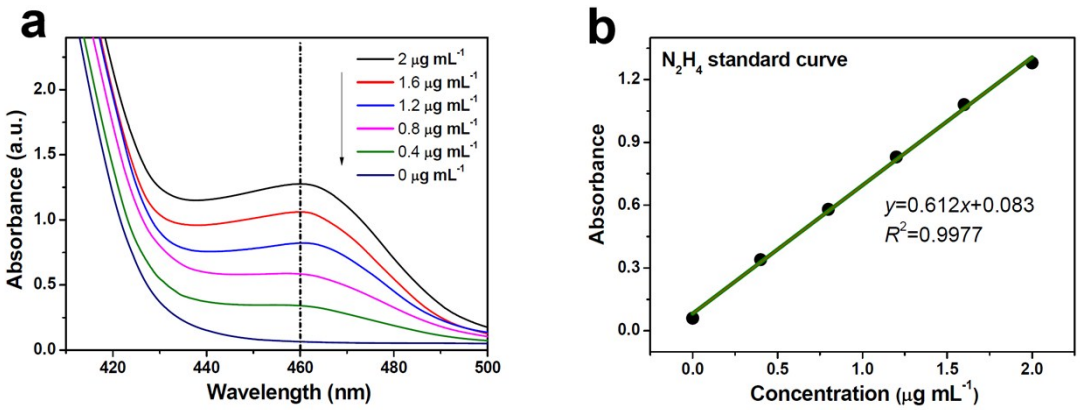

Fig. S7. (a) UV-Vis absorption spectra of N_2H_4 assays after incubated for 20 min at ambient conditions. (b) Calibration curve used for calculation of N_2H_4 concentrations.

Determination of N_2H_4

The N_2H_4 concentration was quantitatively determined by a method of Watt and Chrisp[7, 8]. Typically, 5 mL of electrolyte was removed from the electrochemical reaction vessel. The 330 mL of color reagent containing 300 mL of ethyl alcohol, 5.99 g of $C_9H_{11}NO$ and 30 mL of HCl were prepared, and 5 mL of color reagent was added into the electrolyte. After stirring for 10 min, the UV-Vis absorption spectrum was measured and the concentration-absorbance curves were calibrated by the standard N_2H_4 solution with a serious of concentrations (Fig. S7a). As shown in Fig. S7b, the calibration curve shows a good linear relationship (y=0.612x+0.083, R^2 =0.9977).

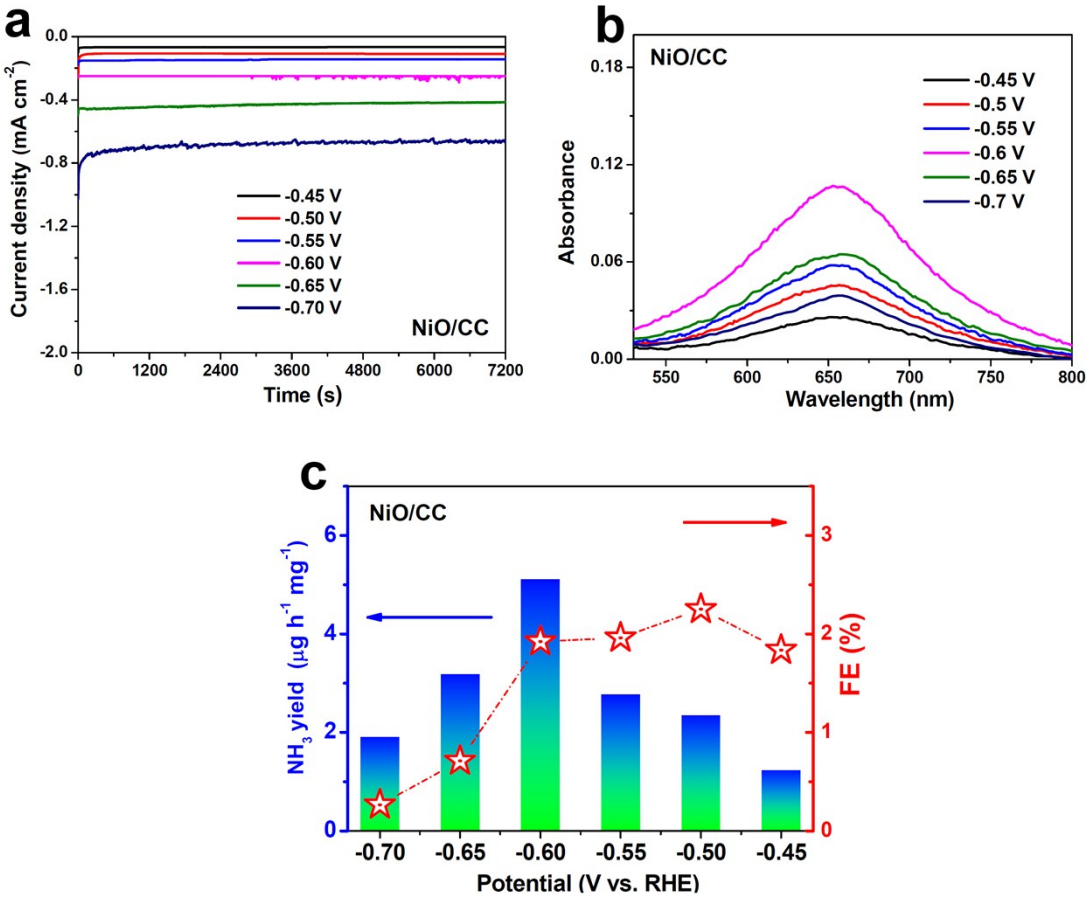

Fig. S8. (a) Time-dependent current densities of NiO/CC after 2 h NRR electrolysis at various potentials, and corresponding (b) UV−vis absorption spectra of the electrolytes (stained with indophenol indicator) and (c) obtained NH_3 yields and FEs.

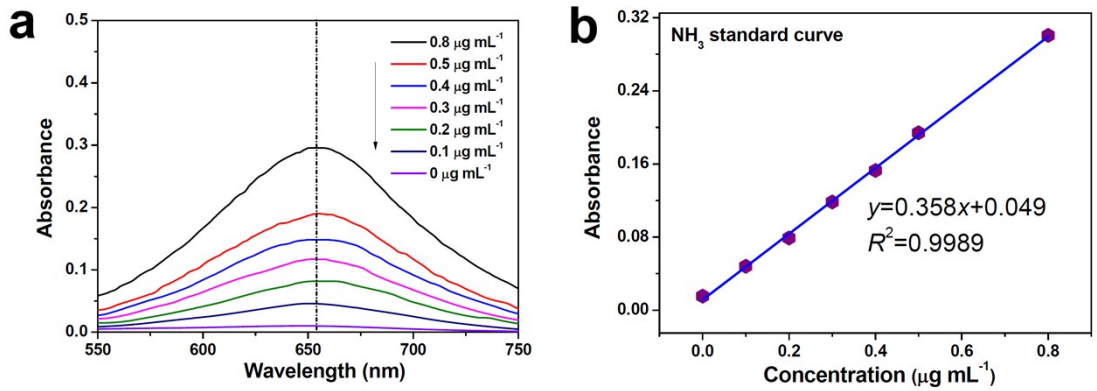

Fig. S9. (a) UV-Vis absorption spectra of indophenol assays with NH_4Cl in 0.1 M HCl after incubated for 2 h at ambient conditions. (b) Calibration curve used for calculation of NH_3 concentrations.

Determination of NH_3 in 0.1 M HCl

The concentration of produced NH_3 in 0.1 M HCl was quantitatively determined by an indophenol blue method[9]. Briefly, 2 mL of electrolyte was removed from the electrochemical reaction vessel. The 2 mL of 1 M NaOH solution (containing 5 wt% $C_7H_6O_3$ and 5 wt% $Na_3C_6H_5O_7$), 1 mL of 0.05 M NaClO and 0.2 mL of 1 wt% $C_5FeN_6Na_2O$ were respectively added into the electrolyte. After standing for 2 h, the UV-Vis absorption spectrum was measured and the concentration-absorbance curves were calibrated by the standard N_2H_4 solution with a serious of concentrations (Fig. S10a). As shown in Fig. S10b, the calibration curve shows a good linear relationship (y=0.358x+0.049, R^2 =0.9989). The calculations of NH_3 yield and FE use the same equations shown in Eq. (S1) and Eq. (S2), respectively.

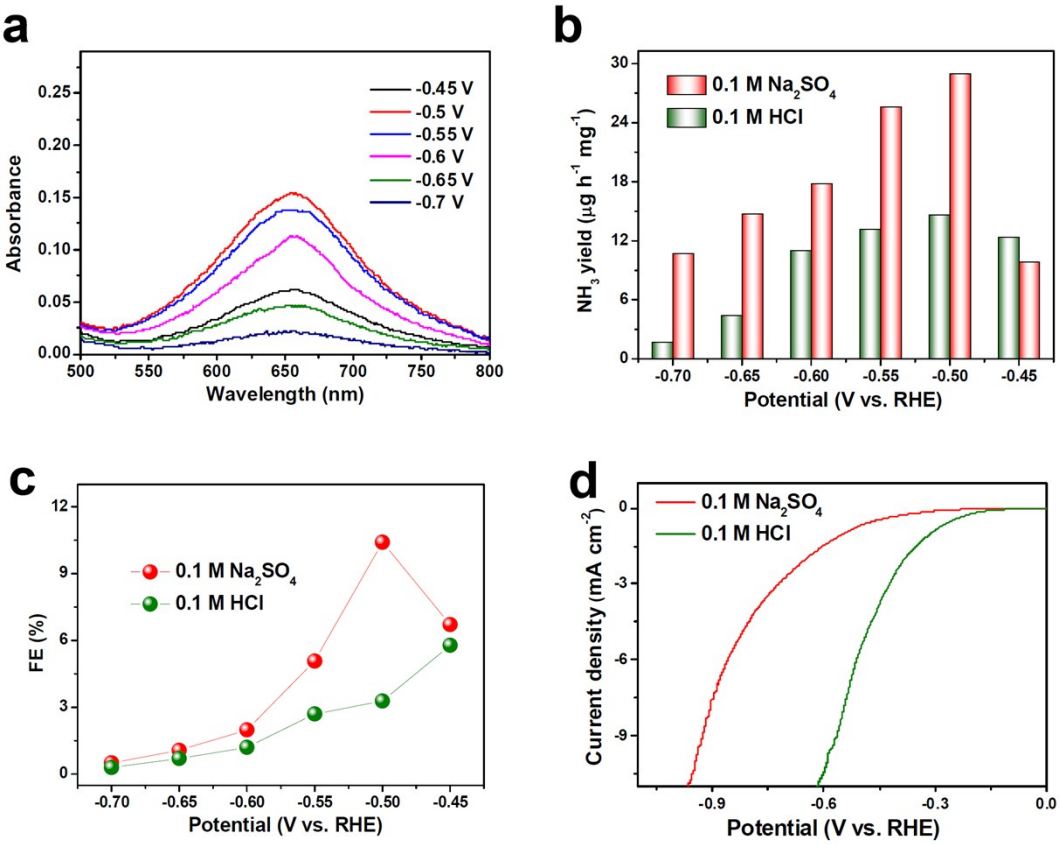

Fig. S10. (a) UV-Vis absorption spectra of the electrolytes after 2 h electrolysis in 0.1 M HCl on P-NiO/CC at various potentials. (b) NH_3 yields and (c) FEs of P-NiO/CC after catalyzing in 0.1 M HCl and 0.1 M Na_2SO_4 at various potentials. (d) LSV curves of P-NiO/CC in 0.1 M HCl and 0.1 M Na_2SO_4.

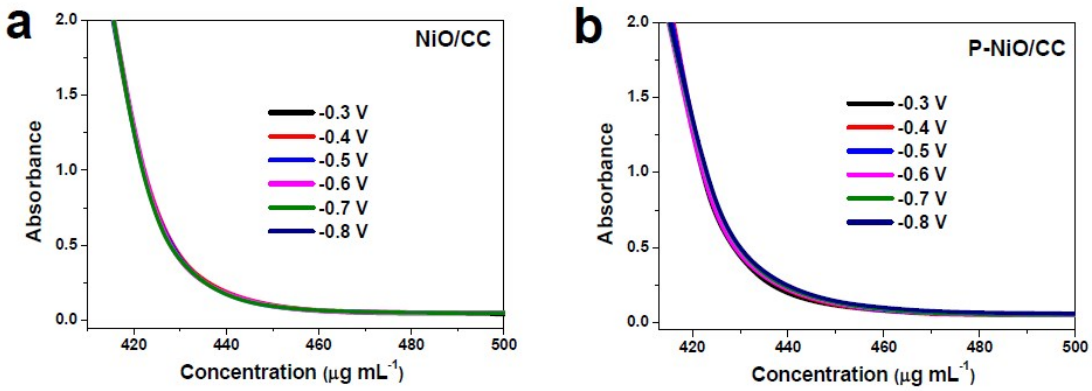

Fig. S11. UV-Vis spectra of the electrolytes (estimated by the method of Watt and Chrisp) after 2 h electrolysis on (a) NiO/CC and (b) P-NiO/CC at various potentials.

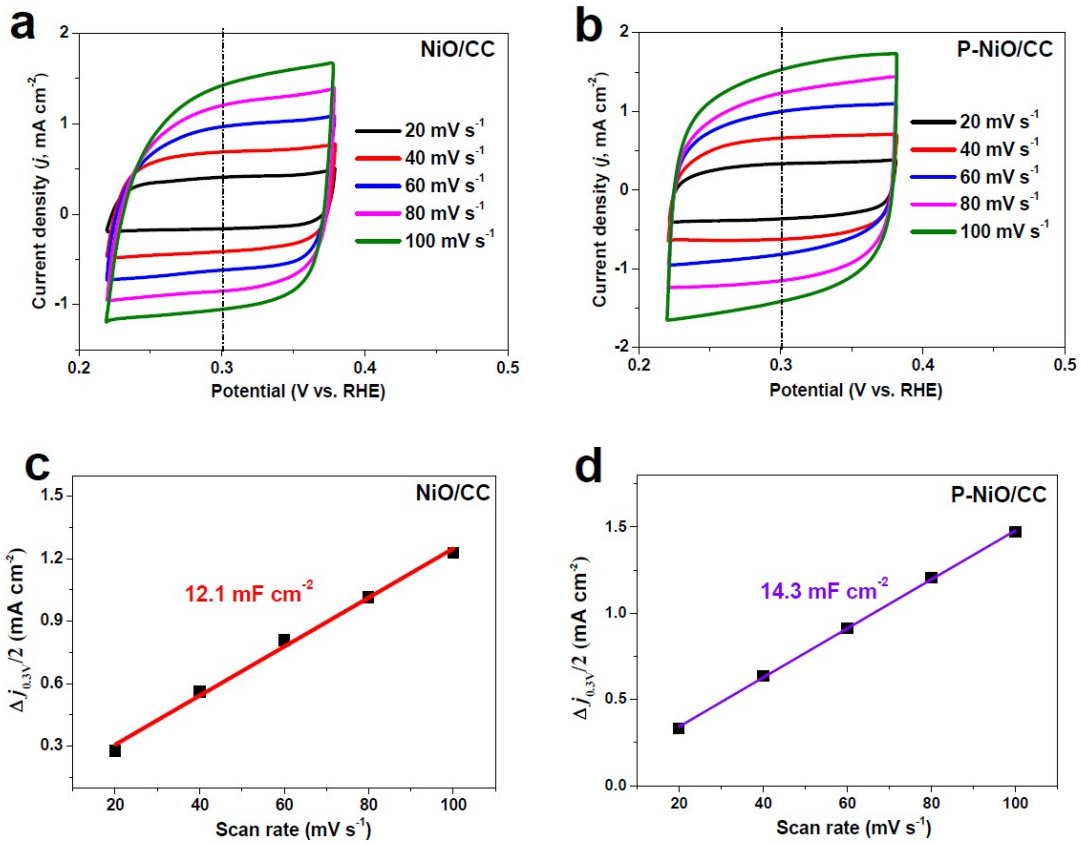

Fig. S12. CV curves of (a) NiO/CC and (b) P-NiO/CC at various scan rates, and corresponding plots of current density differences ($\Delta j/2$) vs. scan rate at 0.3 V vs. RHE.

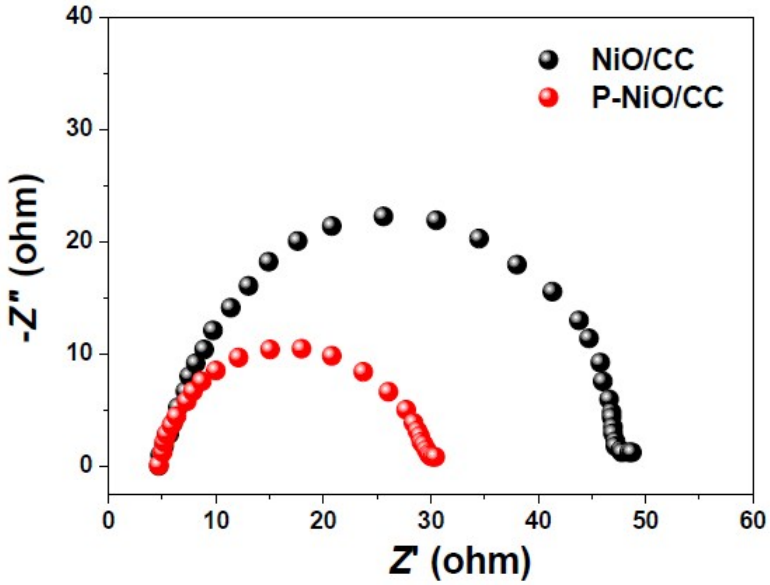

Fig. S13. Electrochemical impendence spectra of NiO/CC and P-NiO/CC.

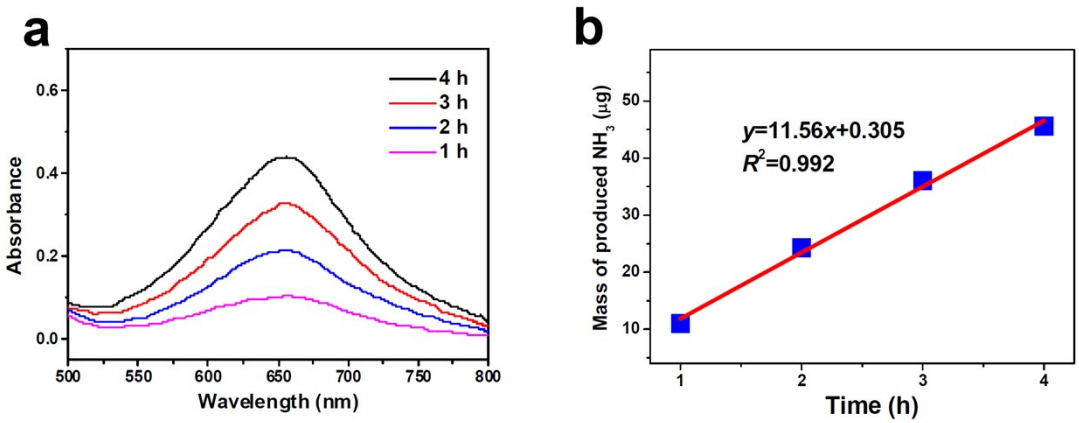

Fig. S14. (a) UV-Vis absorption spectra of the electrolytes after electrolysis at various times on P-NiO/CC at -0.5 V, and (b) corresponding mass of produced NH_3.

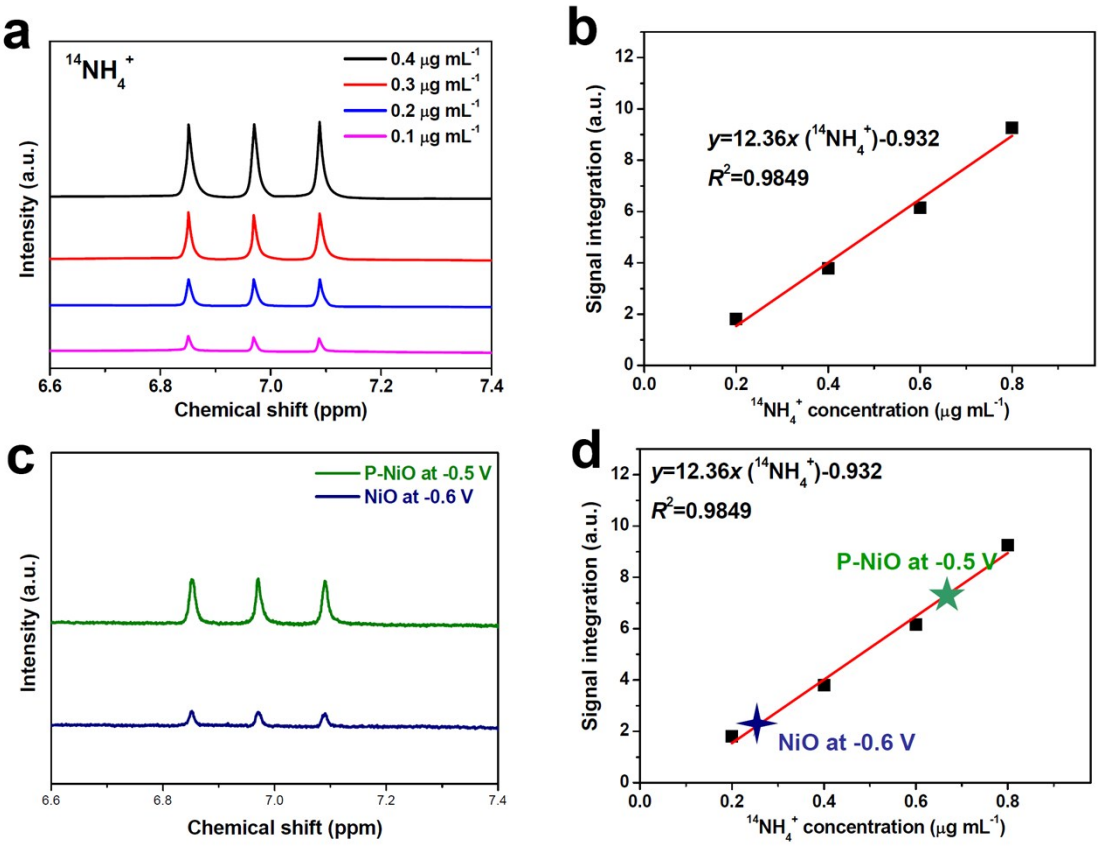

Fig. S15. (a) ^{1}H NMR spectra of $^{14}NH_4^+$ standard samples with different concentrations. (b) The corresponding calibration curve of $^{14}NH_4^+$ concentration vs. peak area intensity based on the ^{1}H NMR spectra. (c) NMR spectra of the electrolytes after catalyzing on NiO/CC at -0.6 V and P-NiO/CC at -0.5 V for 2h. (d) The $^{14}NH_4^+$ concentrations of electrolytes quantitatively determined by the calibration curve (b).

Given that the peak area of NMR spectra correlates well with the NH_3 concentration, the concentration of $^{14}NH_4^+$ can be quantitatively determined by the isotopic labelling measurements[10, 11]. As shown in Fig. S15b, the calculated peak areas show a good linear relation with $^{14}NH_4^+$ concentrations of standard samples. As depicted in Fig. S15d, the measured NiO/CC and P-NiO/CC samples exhibit the $^{14}NH_4^+$ concentration of 0.248 μg/mL and 0.662 μg/mL, respectively, which match well with those (0.233 μg/mL and 0.635 μg/mL) obtained by the indophenol blue method with reasonable experimental errors.

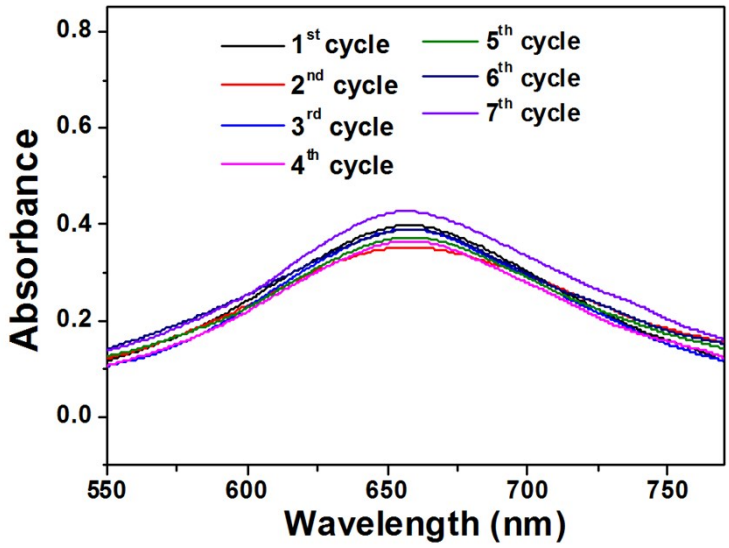

Fig. S16. UV-Vis absorption spectra of working electrolytes on P-NiO/CC (each for 2 h electrolysis at -0.5 V) for seven cycles.

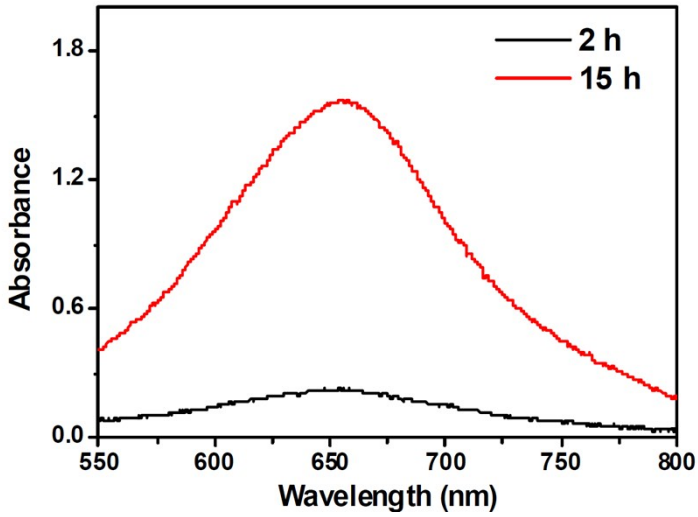

Fig. S17. UV-Vis absorption spectra of working electrolytes after 2 h and 15 h electrolysis on P-NiO/CC at -0.5 V.

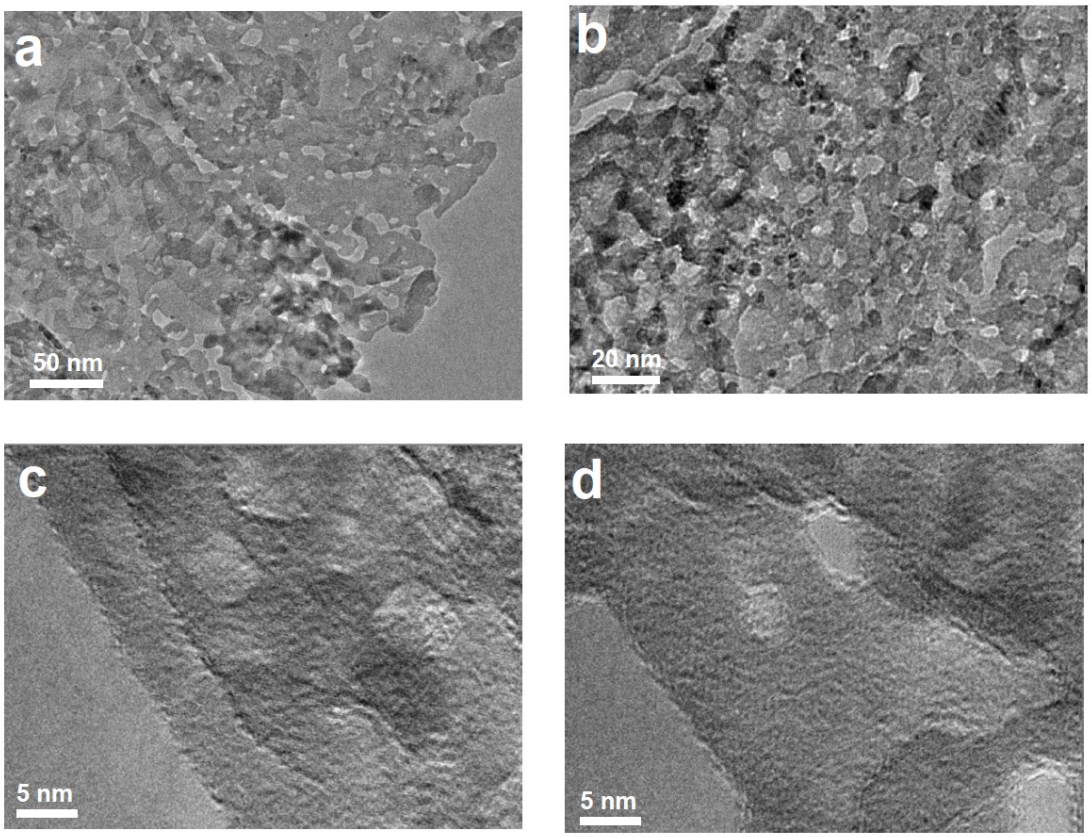

Fig. S18. Morphologies of P-NiO/CC after stability test.

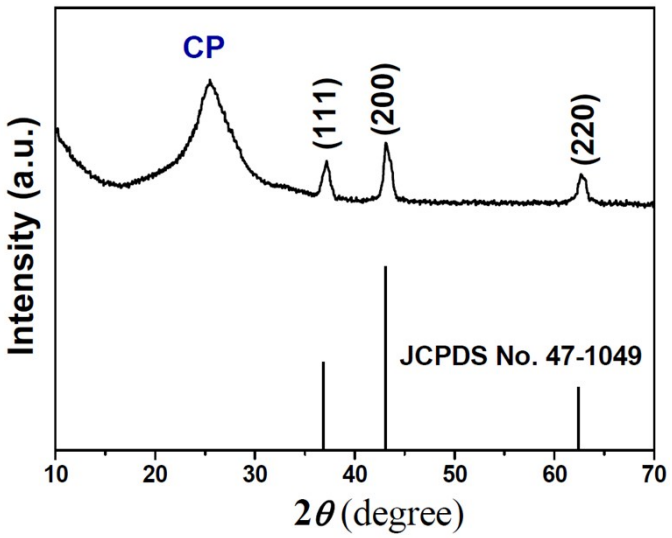

Fig. S19. XRD pattern of P-NiO/CC after stability test.

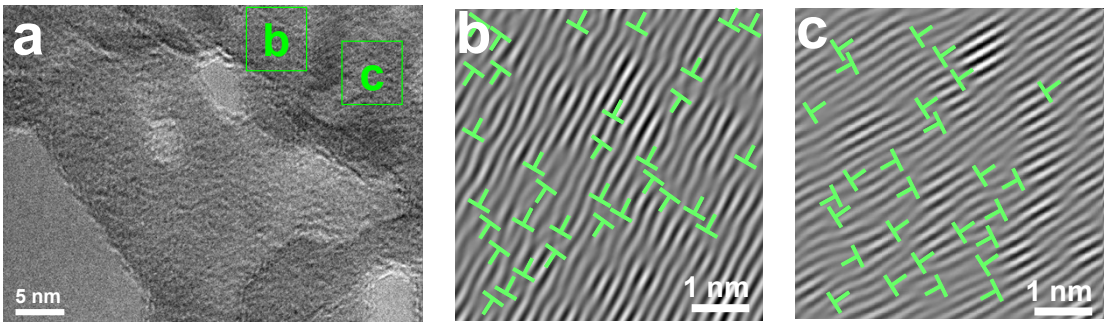

Fig. S20. (a) HRTEM image and (b, c) corresponding IFFT images (recorded at marked b and c regions in (a)) of P-NiO/CC after stability test. “T” shaped symbols stand for the dislocations.

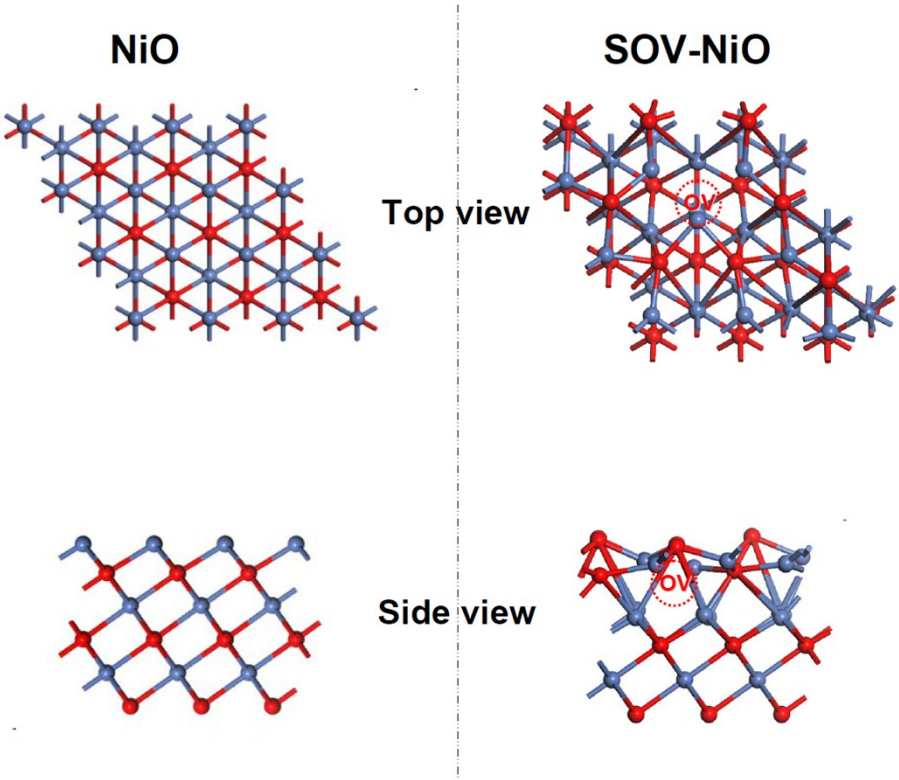

Fig. S21. Side-view and top-view images of the optimized slabs of pristine NiO and SOV-NiO (with single OV). Blue grey and red spheres are Ni and O atoms, respectively.

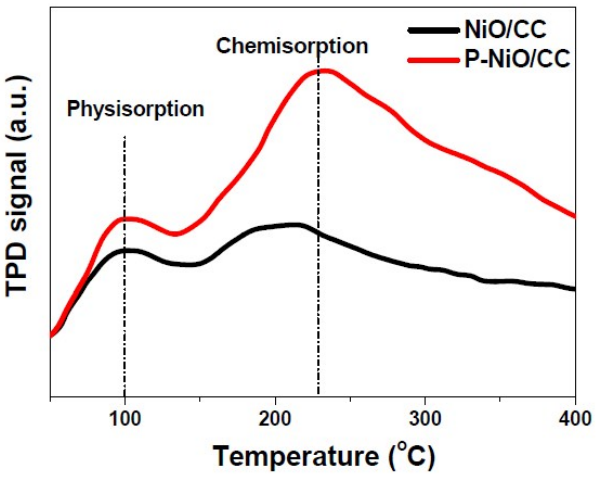

Fig. S22. N_2-TPD spectra of NiO/CC and P-NiO/CC

As shown in Fig. S22, the TPD spectra show the double peaks where the peak at temperatures of 100 °C is assigned to N_2 physisorption and the peak at 200~250 °C corresponds to N_2 chemisorption. As seen, both NiO/CC and P-NiO/CC show a pronounced physisorption peak, whereas P-NiO/CC exhibits a much intensified chemisorption peak over NiO/CC, indicating that P-NiO/CC possesses a stronger N_2 adsorption ability than NiO/CC.

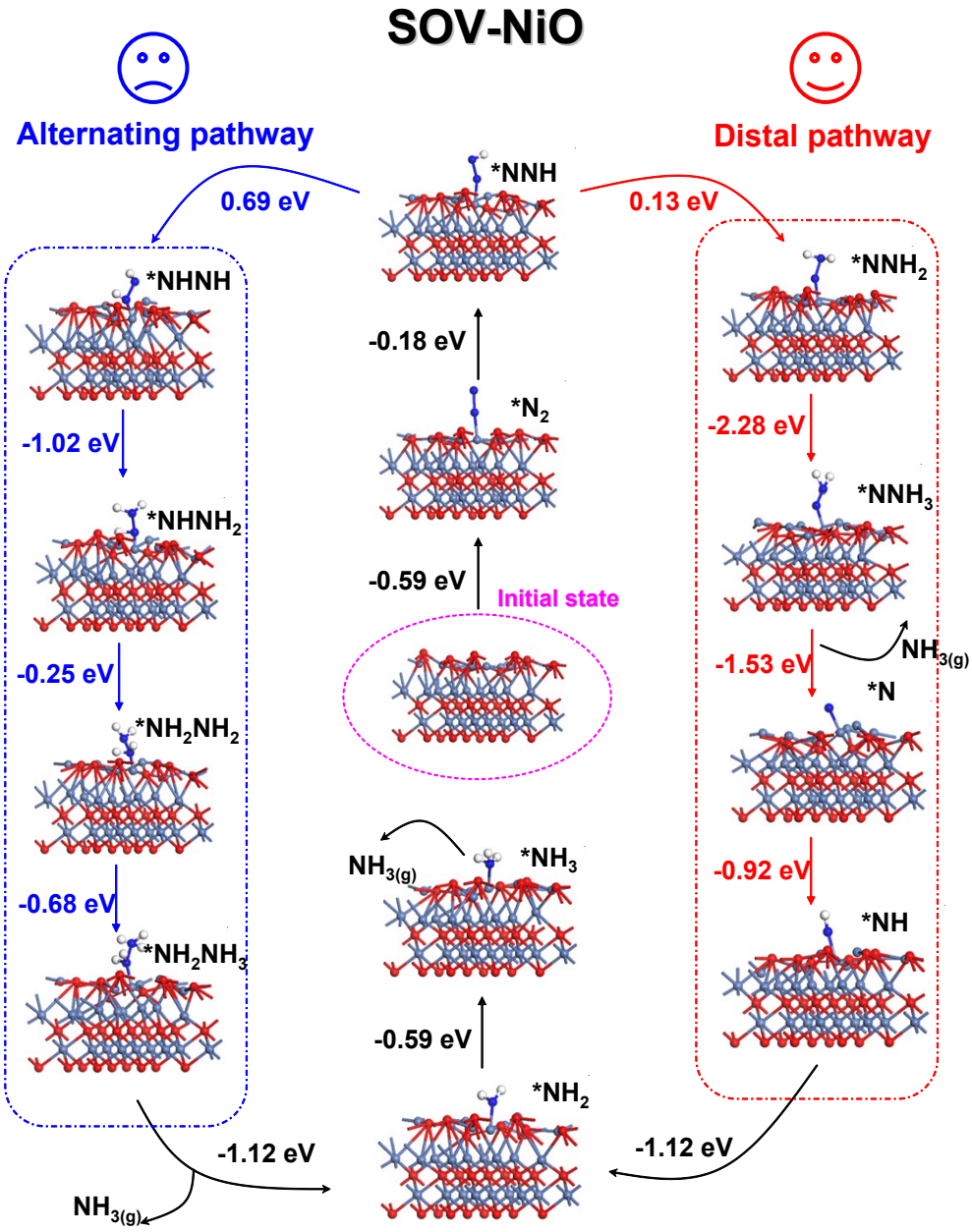

Fig. S23. Optimized structures and calculated ΔG of the reaction intermediates in distal and alternating associative pathways on SOV-NiO. Blue, blue grey, red and white spheres are N, Ni, O and H atoms, respectively.

As shown in Fig. S23, the formation energies of distal intermediates, *NNH_2 (0.13 eV), *NNH_3 (-2.28 eV), *N (-1.53 eV) and *NH (-0.92 eV), are all lower than those of the corresponding alternating intermediates, *NHNH (0.69 eV), *$NHNH_2$ (-1.02 eV), *NH_2NH_2 (-0.25 eV) and *NH_2NH_3 (-0.68 eV). The RDS of distal pathway (*NNH_3 → *N, 0.75 eV) is also lower than that of alternating pathway (*NNH → *NHNH, 0.87 eV), suggesting that the distal route is energetically more favorable than alternating route for SOV-NiO.

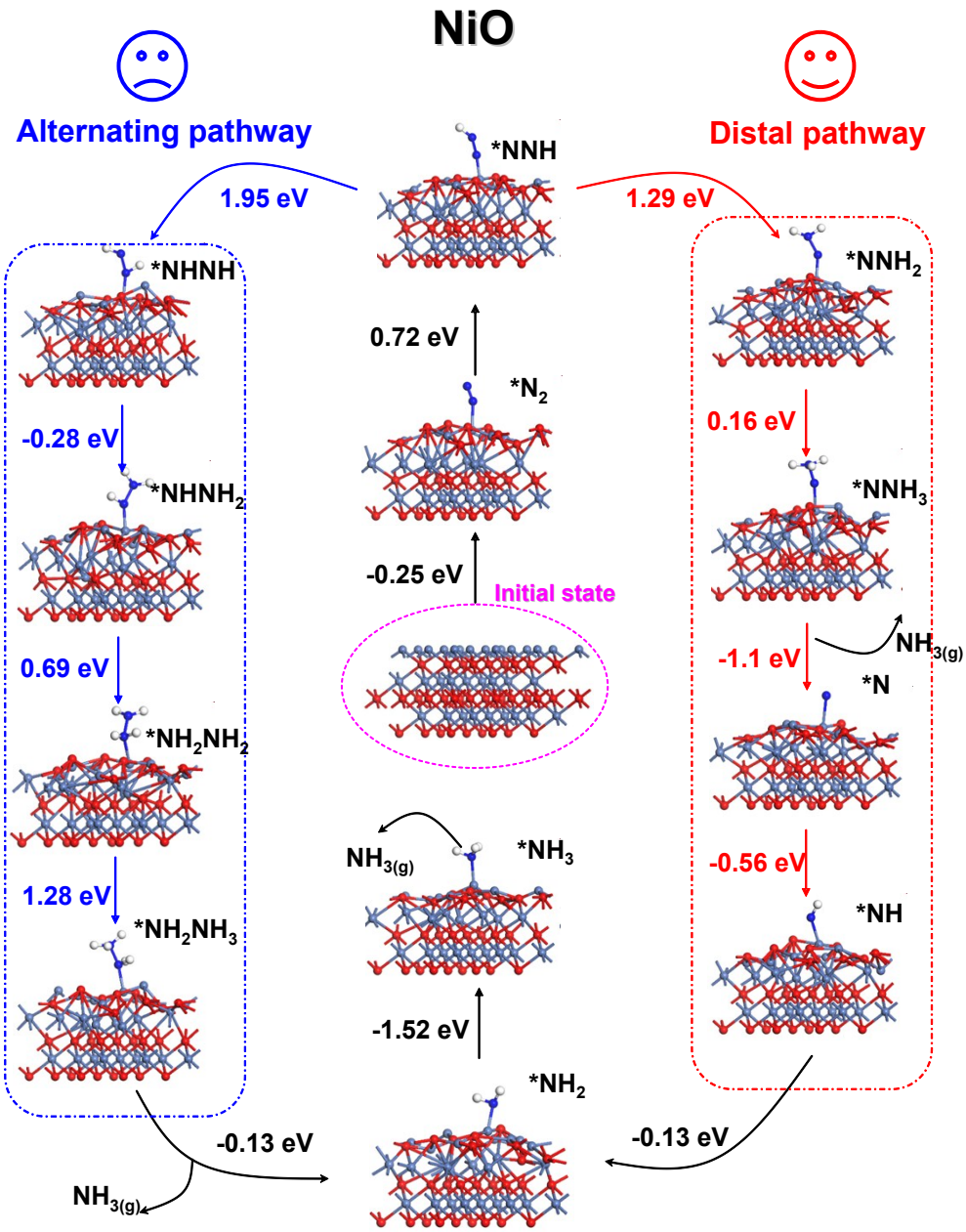

Fig. S24. Optimized structures and calculated Δ*G* of the reaction intermediates in distal and alternating associative pathways on pristine NiO. Blue, blue grey, red and white spheres are N, Ni, O and H atoms, respectively.

As shown in Fig. S24, the alternating route to generate *NHNH, *NH_2NH_2 and *NH_2NH_3 demands the formation energies of 1.95 eV, 0.69 eV and 1.28 eV, respectively, which are much higher than those of corresponding *NNH (1.29 eV), *NNH_2 (-1.1 eV) and *NNH_3 (-0.56 eV) intermediates formed in the distal route. The RDS of distal pathway (*N_2 → *NNH, 0.97 eV) is also lower than that of alternating pathway (*NNH → *NHNH, 1.23 eV), suggesting that the NRR preferentially proceeds through distal route for NiO.

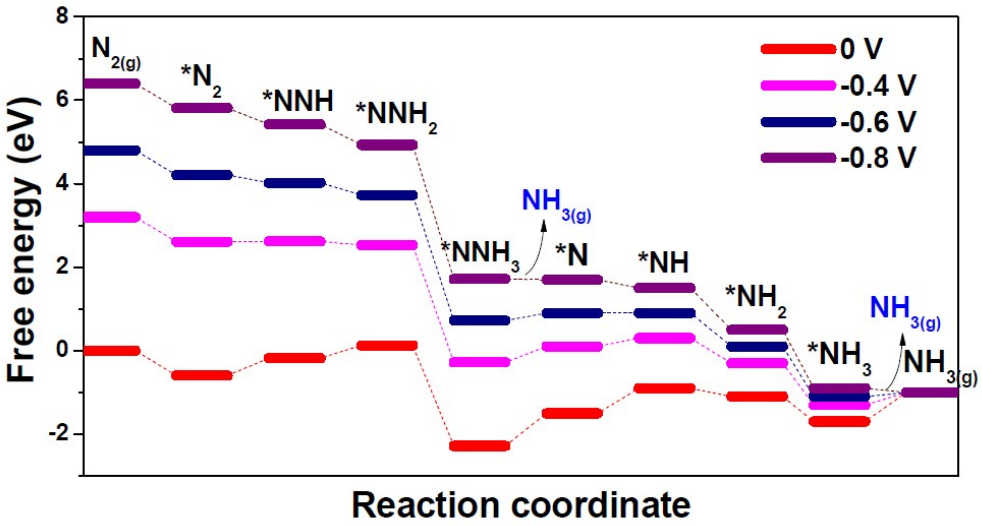

Fig. S25. Free energy diagrams of distal NRR pathway on SOV-NiO at zero and applied energies of -0.4 V, -0.6 V and -0.8 V.

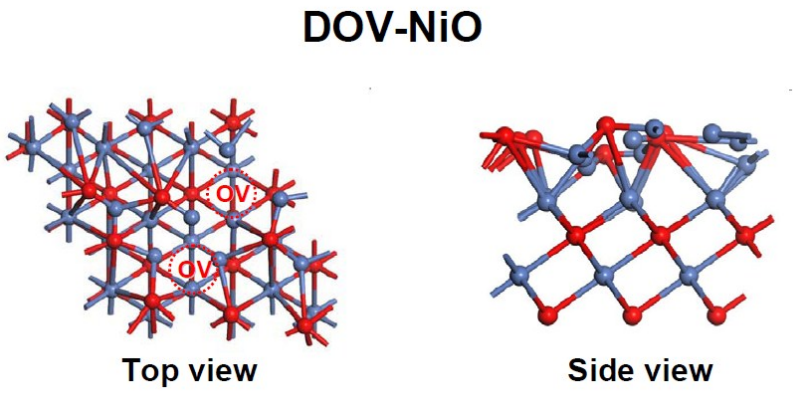

Fig. S26. Side-view and top-view images of optimized slabs of DOV-NiO (with double OVs). Blue grey and red spheres are Ni and O atoms, respectively.

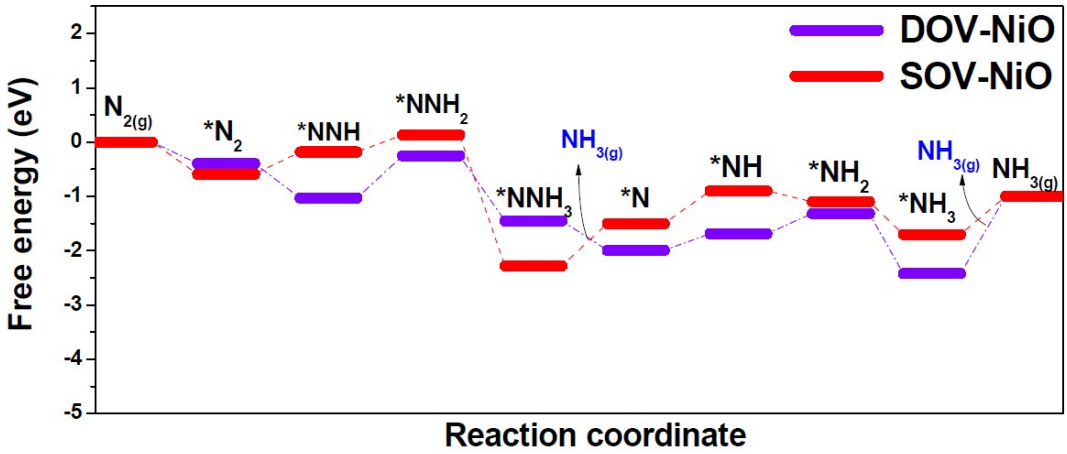

Fig. S27. Free energy diagrams of distal NRR pathway on SOV-NiO and DOV-NiO at zero applied energy.

Table S1. Comparison of NH_3 yield and Faradic efficiency (FE) of recently reported state-of-the-art electrocatalysts at ambient conditions

Catalyst	Electrolyte	Determination method	Potential (V vs RHE)	NH_3 yield	FE (%)	Ref.
Au-TiO_2 sub-nanocluster	0.1 M HCl	Indophenol blue method	-0.2	21.4 μg h^{-1} mg^{-1}	8.11	[12]
Au nanorods	0.1 M KOH	Nessler's reagent method	-0.2	1.65 μg cm^{-2} h^{-1}	4.02	[13]
Amorphous $Pd_{0.2}Cu_{0.8}$/RGO	0.1 M KOH	Indophenol blue method	-0.2	2.8 μg h^{-1} mg^{-1}	0.6	[14]
OV-$BiVO_4$	0.2 M Na_2SO_4	Indophenol blue method	-0.5	8.6 μg h^{-1} mg^{-1}	10.4	[15]
Ru single atoms	0.05 M H_2SO_4	Indophenol blue method	-0.2	120.9 μg h^{-1} mg^{-1}	29.6	[16]
PEBCD/C	0.5 M Li_2SO_4	Nessler's reagent method	-0.5	2.58×10^{-11} mol h^{-1} cm^{-2}	2.85	[17]
Mo_2C/C	0.5 M Li_2SO_4	Nessler's reagent method	-0.3	11.3 μg h^{-1} mg^{-1}	7.8	[10]
MXene	0.5 M Li_2SO_4	Nessler's reagent method	-0.1	4.7 μg cm^{-2} h^{-1}	5.78	[18]
Black phosphorus	0.01 M HCl	Indophenol blue method	-0.6	31.37 μg h^{-1} mg^{-1}	5.07	[11]
B_4C nanosheet	0.1 M HCl	Indophenol blue method	-0.75	26.57 μg h^{-1} mg^{-1}	15.95	[19]
MoS_2/CC	0.1 M Na_2SO_4	Indophenol blue method	-0.5	8.08×10^{-11} mol s^{-1} cm^{-2}	1.17	[7]
Hollow Cr_2O_3 microspheres	0.1 M Na_2SO_4	Indophenol blue method	-0.9	25.3 μg h^{-1} $mg^{-1}_{cat.}$	6.78	[20]
Defect-rich MoS_2 nanoflower	0.1 M Na_2SO_4	Indophenol blue method	-0.4	29.28 μg h^{-1} mg^{-1}	8.34	[21]
Nb_2O_5 nanofibers	0.1 M HCl	Indophenol blue method	-0.55	43.6 μg h^{-1} mg^{-1}	9.26	[22]
Mn_3O_4 nanocubes	0.1 M Na_2SO_4	Indophenol blue method	-0.8	11.6 μg h^{-1} mg^{-1}	3	[23]
TiO_2/CC	0.1 M Na_2SO_4	Indophenol blue method	-0.7	9.16×10^{-11} mol s^{-1} cm^{-2}	2.5	[24]
$Ti_3C_2T_x$ nanosheets	0.1 M HCl	Indophenol blue method	-0.4	20.4 μg h^{-1} mg^{-1}	9.3	[25]
S-doped carbon nanospheres	0.1 M Na_2SO_4	Indophenol blue method	-0.7	19.07 μg h^{-1} mg^{-1}	7.47	[26]
C-doped TiO_2 nanoparticles	0.1 M Na_2SO_4	Indophenol blue method	-0.7	16.22 μg h^{-1} mg^{-1}	1.84	[27]
Boron-doped TiO_2	0.1 M	Indophenol blue	-0.8	14.4	3.4	[28]

	Na_2SO_4	method		μg h^{-1} mg^{-1}		
N-doped carbon spikes	0.25 M $LiClO_4$	Indophenol blue method	-1.19	97.18 μg cm^{-2} h^{-1}	11.56	[29]
$Bi_4V_2O_{11}$-CeO_2 nanofibers	0.1 M HCl	Indophenol blue method	-0.2	23.21 μg h^{-1} mg^{-1}	10.16	[30]
CoP hollow nanocage	1.0 M KOH	Indophenol blue method	-0.4	10.78 μg h^{-1} mg^{-1}	7.36	[31]
Rh nanosheets	0.1 m KOH	Phenolhypochlo-rite method	-0.2	23.88 μg h^{-1} mg^{-1}	0.217	[32]
$VN_{0.7}O_{0.45}$	Nafion	Nessler's reagent method	-0.1	3.31×10^{-10} mol s^{-1} cm^{-2}	5.95	[33]
Mo single atoms	0.1 M KOH	Indophenol blue method	-0.3	34 μg h^{-1} mg^{-1}	14.6	[34]
Polymeric carbon nitride	0.1 M HCl	Indophenol blue method	-0.2	8.09 μg h^{-1} mg^{-1}	11.59	[35]
P-NiO/CC	0.1 M Na_2SO_4	Indophenol blue method	-0.5	29.1 μg h^{-1} mg^{-1}	10.8	This work

Supplementary references

[1]. N. Cheng, L. Qian, J. Tian, X. Sun, Y. He, S. Zhai and A. M. Asiri, *Int. J. Hydrogen Energy*, 2015, **40**, 9866-9871.

[2]. S. J. Clark, M. D. Segall, C. J. Pickard, P. J. Hasnip, M. I. J. Probert, K. Refson and M. C. Payne, *Z. Kristallogr.*, 2005, **220**, 567-570.

[3]. S. Grimme, J. Antony, S. Ehrlich and H. Krieg, *J. Chem. Phys.*, 2010, **132**, 154104.

[4]. Y. Lu, L. Su, J. Qi, S. Lei, B. Liu, Q. Zang, S. Shi and X. Yan, *J. Mater. Chem. A*, 2018, **28**, 13717-13724.

[5]. W. Zhao, M. Bajdich, S. Carey, A. Vojvodic, J. K. Nørskov and C. T. Campbell, *ACS Catal.*, 2016, **6**, 7377-7384.

[6]. A. A. Peterson, *Energy Environ. Sci.*, 2010, **3**, 1311-1315.

[7]. L. Zhang, X. Ji, X. Ren, Y. Ma, X. Shi, Z. Tian, A. M. Asiri, L. Chen, B. Tang and X. Sun, *Adv. Mater.*, 2018, **30**, 1800191.

[8]. G. W. Watt and J. D. Chrisp, *Anal. Chem.*, 1952, **24**, 2006-2008.

[9]. D. Zhu, L. Zhang, R. E. Ruther and R. J. Hamers, *Nat. Mater.*, 2013, **12**, 836.

[10]. H. Cheng, L. X. Ding, G. F. Chen, L. Zhang, J. Xue and H. Wang, *Adv. Mater.*, 2018, **30**, 1803694.

[11]. L. L. Zhang, L. X. Ding, G. F. Chen, X. F. Yang and H. H. Wang, *Angew. Chem. Int. Edit.*, 2019, **131**, 2638-2642.

[12]. M. M. Shi, D. Bao, B. R. Wulan, Y. H. Li, Y. F. Zhang, J. M. Yan and Q. Jiang, *Adv. Mater.*, 2017, **29**, 1606550.

[13]. D. Bao, Q. Zhang, F. L. Meng, H. X. Zhong, M. M. Shi, Y. Zhang, J. M. Yan, Q. Jiang and X. B. Zhang, *Adv. Mater.*, 2017, **29**, 1604799.

[14]. M. M. Shi, D. Bao, S. J. Li, B. R. Wulan, J. M. Yan and Q. Jiang, *Adv. Energy. Mater.*, 2018, **8**, 1800124.

[15]. J. X. Yao, D. Bao, Q. Zhang, M. M. Shi, Y. Wang, R. Gao, J. M. Yan and Q. Jiang, *Small Methods*, 2018, **3**, 1800333.

[16]. Z. Geng, Y. Liu, X. Kong, P. Li, K. Li, Z. Liu, J. Du, M. Shu, R. Si and J. Zeng, *Adv. Mater.*, 2018, **30**, 1803498.

[17]. G. F. Chen, X. R. Cao, S. Q. Wu, X. Y. Zeng, L. X. Ding, M. Zhu and H. H. Wang, *J. Am. Chem. Soc.*, 2017, **139**, 9771-9774.

[18]. Y. R. Luo, G. F. Chen, L. Ding, X. Z. Chen, L. X. Ding and H. H. Wang, *Joule*, 2019, **3**, 279-289.

[19]. W. Qiu, X.-Y. Xie, J. Qiu, W.-H. Fang, R. Liang, X. Ren, X. Ji, G. Cui, A. M. Asiri and G. Cui, *Nat. Commun.*, 2018, **9**, 3485.

[20]. Y. Zhang, W. Qiu, Y. Ma, Y. Luo, Z. Tian, G. Cui, F. Xie, L. Chen, T. Li and X. Sun, *ACS Catal.*, 2018, **8**, 8540-8544.

[21]. X. Li, T. Li, Y. Ma, Q. Wei, W. Qiu, H. Guo, X. Shi, P. Zhang, A. M. Asiri and L. Chen, *Adv. Energy. Mater.*, 2018, **8**, 1801357.

[22]. J. Han, Z. Liu, Y. Ma, G. Cui, F. Xie, F. Wang, Y. Wu, S. Gao, Y. Xu and X. Sun, *Nano Energy*, 2018, **52**, 264-270.

[23]. X. Wu, L. Xia, Y. Wang, W. Lu, Q. Liu, X. Shi and X. Sun, *Small*, 2018, **14**, 1803111.

[24]. R. Zhang, X. Ren, X. Shi, F. Xie, B. Zheng, X. Guo and X. Sun, *ACS Appl. Mater. Inter.*, 2018, **10**, 28251-28255.

[25]. J. Zhao, L. Zhang, X.-Y. Xie, X. Li, Y. Ma, Q. Liu, W.-h. Fang, X. Shi, G. Cui and X. Sun, *J. Mater. Chem. A*, 2018, **6**, 24031-24035.

[26]. L. Xia, X. Wu, Y. Wang, Z. Niu, Q. Liu, T. Li, X. Shi, A. M. Asiri and X. Sun, *Small Methods*, 2018, **3**, 1800251.

[27]. Y. Wang, Q. Pan, B. Zhong, Y. Luo, G. Cui, X.-D. Guo and X. Sun, *Nanoscale Adv.*, 2019, **1**, 961-964.

[28]. Y. Wang, K. Jia, Q. Pan, Y. Xu, Q. Liu, G. Cui, X. Guo and X. Sun, *ACS Sustain. Chem. Eng.*, 2019, **7**, 117-122.

[29]. Y. Song, D. Johnson, R. Peng, D. K. Hensley, P. V. Bonnesen, L. Liang, J. Huang, F. Yang, F. Zhang and R. Qiao, *Sci. Adv.*, 2018, **4**, e1700336.

[30]. C. Lv, C. Yan, G. Chen, Y. Ding, J. Sun, Y. Zhou and G. Yu, *Angew. Chem. Int. Edit.*, 2018, **130**, 6181-6184.

[31]. W. Guo, Z. Liang, J. Zhao, B. Zhu, K. Cai, R. Zou and Q. Xu, *Small Methods*, 2018, **2**, 1800204.

[32]. H. M. Liu, S. H. Han, Y. Zhao, Y. Y. Zhu, X. L. Tian, J. H. Zeng, J. X. Jiang, B. Y. Xia and Y. Chen, *J. Mater. Chem. A*, 2018, **6**, 3211-3217.

[33]. X. Yang, J. Nash, J. Anibal, M. Dunwell, S. Kattel, E. Stavitski, K. Attenkofer, J. G. Chen, Y. Yan and B. Xu, *J. Am. Chem. Soc.*, 2018, **140**, 13387-13391.

[34]. L. Han, X. Liu, J. Chen, R. Lin, H. Liu, F. Lu, S. Bak, Z. Liang, S. Zhao and E. Stavitski, *Angew. Chem. Int. Edit.*, 2018, **58**, 2321-2325.

[35]. C. Lv, Y. Qian, C. Yan, Y. Ding, Y. Liu, G. Chen and G. Yu, *Angew. Chem. Int. Edit.*, 2018, **57**, 10246-10250.